

**CHARACTERIZATION OF SHALLOW SHEAR
WAVE VELOCITY STRUCTURES IN
SOUTHWESTERN UTAH**

by

Simin Huang

A thesis submitted to the faculty of
The University of Utah
in partial fulfillment of the requirements for the degree of

Master of Science

in

Geophysics

Department of Geology and Geophysics

The University of Utah

May 2011

Copyright © Simin Huang 2011

All Rights Reserved

ABSTRACT

Key to understanding local site conditions is the shallow shear-wave velocity structure. In the southwest corner of Utah near the rapidly growing urban areas of St. George and Cedar City, there currently exist no available data for characterizing site class units. This region has the potential for experiencing magnitude 6.5 or larger events. The University of Utah Seismograph Stations recently installed an urban strong-motion network in the region and there is also a need to characterize the shallow velocity structures at the sensor locations. In order to determine the shallow shear-wave velocity structure in and near St. George and Cedar City, we collected microtremor data using an array of four (three-component) broadband seismometers at six sites. We processed these data by (1) calculating the coherency between sensors, (2) calculating the horizontal to vertical spectral ratio (HVSR), and (3) calculating phase velocity dispersion curves. We determine the shallow S-wave velocity structure by a forward modeling approach using the Multimode spatial autocorrelation method (MMSPAC) and comparing predicted Rayleigh wave fundamental mode ellipticity curves to HVSR data. S-wave velocity models obtained at all sites seem reasonable given what is known of the geology with the exception of one site near Cedar City. The average S-wave velocity in the upper 30 meters (V_s30) is between 360 and 760 m/s for all six sites. This is the velocity range corresponding to NEHRP site class unit C.

To my parents, Pingnan Huang and Guiying Zeng

CONTENTS

ABSTRACT	iii
LIST OF FIGURES.....	vi
ACKNOWLEDGMENTS.....	viii
CHAPTERS	
1. INTRODUCTION	1
2. THEORY	4
3. DATA ACQUISITION.....	6
4. DATA PROCESSING	11
5. FORWARD MODELING S-WAVE VELOCITY STRUCTURE	19
6. RESULTS	21
7. CONCLUSIONS	25
APPENDIX: SUPPLEMENTAL FIGURES.....	26
REFERENCES	37

LIST OF FIGURES

3.1	Geologic and site location map for the study area. The overall study region is shown in the inset in the lower right corner. The primary study area encompasses the cities of Cedar City and St. George, Utah, as outlined by the red box. In the main panel the colors indicate the age of the geologic units. Quaternary faults are shown as solid lines and the two most prominent faults in the area are labeled (the Hurricane and Washington Faults). The locations of the seismic arrays we deployed in this study are shown as red bursts and seismic stations as either yellow circles (strong-motion) or diamonds (broadband).	8
3.2	Array geometry of the microtremor survey. Three of the four sensors were placed at the vertexes of an equilateral triangle with the fourth sensor placed at the center. The sensors are deployed three times at each site with a different distance between the center sensor and the outer sensors in each case. Distance between the station at the center and at each vertex was set to 10 m, 30 m and 90 m. Analysis between sensors can be carried out in two configurations (upper left panel): (1) between the center sensor and each outer sensor (radius = R1), (2) between each of the outer sensors (radius = R2).	10
4.1	Observed coherencies versus theoretical coherencies determined using the method of MMSPAC. Black thick lines are the observed coherency curves, red lines are the theoretical coherency curves for the fundamental mode, light blue lines are the theoretical coherency curves for the first higher mode. The gray thin line is the imaginary part of the observed coherency. Each column represents measurements at a single site (CVMS, N7223, or RES) at three different distances. The top two rows show measurements in R1 (see Figure 3.2) and the bottom row shows measurements in R2. . . .	14
4.2	Horizontal to vertical spectral ratios (HVSR) compared to theoretical ellipticity curves predicted for two models. Gray thin line is HVSR of data from a station at 10 m, 30 m, and 90 m distances. Gray dashed line is predicted ellipticity for the models determined using MMSPAC, black thick line is predicted ellipticity for the models modified to best fit the HVSR data. . . .	15
4.3	Phase velocity dispersion curves of data and models. Black thick line is phase velocity calculated using the traditional SPAC method, gray dashed lines are phase velocity dispersion curves for models determined using MMSPAC, black thin lines are phase velocity dispersion curves for models modified to fit the HVSR data.	16

4.4	Observed coherencies versus theoretical coherencies determined using the modified MMSPAC models. Black thick lines are the observed coherency curves, red lines are the theoretical coherency curves for the fundamental mode, light blue lines are the theoretical coherency curves for the first higher mode. The gray thin line is the imaginary part of the observed coherency. Each column represents measurements at a single site (CVMS, N7223, or RES) at three different distances. The top two rows show measurements in a R1 configuration (see Figure 3.2) and the bottom row shows measurements in a R2 configuration.	17
4.5	Shear-wave velocity models. Models for each of the six sites are shown for the two techniques used in this study. Gray lines show models determined using MMSPAC and black lines show models modified to have the ellipticity fit the HVSR. In each case the S-wave velocity models are truncated at the lowest resolvable depth.	18
A.1	Site CCH	27
A.2	Site CCP	28
A.3	Site CVMS	29
A.4	Site FRS	30
A.5	Site RES	31
A.6	Site CCH	32
A.7	Site CCP	33
A.8	Site CVMS	34
A.9	Site FRS	35
A.10	Site RES	36

ACKNOWLEDGMENTS

I would like to thank Dr. Michael Thorne, Dr. Kris Pankow, and my committee member Dr. Aurel Trandafir for their help, advice, and constructive criticism. I also thank Bill Lund and Tyler Knudson for helping us with collecting the data and identifying sites of interest, thank Dr. Michael Asten, Dr. W. J .Stephenson, Valerio Poggi for helping me to utilize various programs and software, and Gary Christenson for help in placing the velocity models in context of the local geology. I thank Dr. Gerard Schuster and all my colleagues and friends in University of Utah for encouraging me to continue on with my research. This thesis is dedicated to my parents, Pingnan Huang and Guiying Zeng.

CHAPTER 1

INTRODUCTION

It has long been recognized that local site conditions modify both the amplitude and spectral content of earthquake generated ground motions (e.g., Borchardt, 1970; Singh *et al.*, 1988). In southwestern Utah, the potential influence of site effects became apparent following the 1992 Mw 5.5 (Ritsema and Lay, 1995) St. George earthquake. The minimal ground motion related damage following this earthquake could not be attributed to the magnitude, stress drop, or radiation pattern effects (Pechmann *et al.*, 1995) leaving site conditions as a viable explanation. However, there have been no studies of the local shallow shear-wave velocity structure necessary for characterizing the local site effects. Since the 1992 earthquake, the region in and near St. George has experienced very rapid growth (the population has nearly doubled in the last 10 years, see Governors report, 2010) making the need to better characterize the local site conditions and seismic hazard a priority.

Key to understanding the seismic hazard and predicting earthquake ground motions is the determination of subsurface elastic properties at local sites. Traditionally, characterization of site effects has been achieved using the average shear velocity in the upper 30 m (V_s30) and empirical corrections (e.g., Borchardt, 1994). Recent studies point to the importance of characterizing the velocity profile including depth to bedrock (Cramer, 2009). Though several reliable techniques have been developed to determine the shallow shear velocity structure many are either too expensive or are too intrusive for the urban environment. Techniques that utilize microtremors have recently become popular for characterizing the shallow velocity structure in urban settings (e.g., Okada, 2003; Louie, 2001).

Microtremors are ambient ground vibrations attributable to both natural phe-

nomenon like ocean waves and storms ($f < 1$ Hz) and cultural noise ($f > 1$ Hz) such as traffic and machinery (e.g., Okada, 2003). Microtremors are continuous, low-amplitude waves that are dominated mostly by surface waves (e.g., Okada, 2003). Though microtremors vary with time and location, for short duration and small changes in position, the energy and frequency content in microtremors is generally constant, so that the waves may be considered stationary in time.

One method for utilizing microtremor data for determining S-wave velocity profiles is spatial autocorrelation (SPAC), which requires the deployment of an array of seismic sensors. SPAC was first proposed by Aki (1957), who deduced that a Love or Rayleigh wave phase velocity dispersion curve for the fundamental mode could be determined from the azimuthally averaged coherency of data acquired from a circular seismic array. Since Aki's original formulation, SPAC has been further developed to utilize different array geometries (Okada, 2003; Asten, 2004; Chávez-García *et al.*, 2006), to allow for temporal, as well as azimuthal averaging (Chávez-García *et al.*, 2005), and to distinguish Love and Rayleigh wave contributions (Köhler *et al.*, 2007). In another development, SPAC has been expanded to look at higher modes, and is termed multimode SPAC (MMPAC; Asten, 2006). This technique uses direct curve fitting between the observed and modeled coherency instead of the inversion of dispersion curves to determine the velocity model. Velocity models determined using the MMSPAC technique compare well with models determined from several other methods such as Suspension PS velocity logger (Boore and Asten, 2008).

A second method for analyzing microtremor data is the analysis of horizontal-to-vertical spectral ratios (HVSr). The ratio is calculated between the Fourier amplitude spectra of the average of the horizontal components and the vertical component. Depending on the contribution of body waves, peaks in these ratios may be interpreted as the fundamental resonance frequency for the soil (Nogoshi and Igrashi, 1971; Nakamura, 1989, 1996, 2000). Alternatively these ratios may be interpreted in terms of the ellipticity of the Rayleigh wave (Fäh *et al.*, 2003) In this paper, we show shear-wave velocity modeling results from analysis of microtremor data collected at six sites in southwestern Utah. For each site, we use MMSPAC

to determine the shear-wave velocity model, refine this model by analysis of the HVSR data, and compare the resulting models to dispersion curves determined using traditional SPAC analysis. The resulting models are discussed in relation to what is known about the local geology.

CHAPTER 2

THEORY

Aki (1957) showed that for spatially uncorrelated waves that are stationary in space and time, the real part of the azimuthally averaged coherency of the power spectrum for vertical component data is related to the Rayleigh wave phase velocity by a Bessel function (J_0) of the first kind of zero order:

$$c(f) = J_0 \left(\frac{2\pi fr}{V(f)} \right) = J_0(rk) \quad (2.1)$$

where f is frequency, r is the array dimension, $V(f)$ is the phase velocity as a function of frequency, and k is the wavenumber. Thus a phase velocity dispersion curve can be determined by correlating the shape (maximum and minimums) of the coherency curve to the Bessel function. As originally developed by Aki (traditional SPAC) the correlation is restricted to the frequencies between the first maximum and first minimum. This restricts the analysis to the fundamental mode.

Ideally, due to the stochastic nature of the noise field, the azimuthally averaged coherency is real. However, as a consequence of array geometry and distribution of noise sources, there is usually an imaginary component in the coherency. The amplitude of the imaginary component can be used to assess the degree to which the basic assumptions are met and whether the data can be modeled.

In Multimode SPAC (MMSPAC; Asten, 2006), the full coherency curve (instead of just those frequencies between the first maximum and first minimum) are utilized. In this method, modeled SPAC curves are generated for a given velocity structure by calculating theoretical phase velocity dispersion curves for multiple modes of the Rayleigh wave. These synthetic SPAC curves are then compared to the coherency

of the power spectrum in the data. This is a forward modeling process where the velocity model (primarily layer thickness and shear-wave velocity) is modified at each step to better fit the data. An advantage of this method over traditional SPAC is the ability to fit higher-mode energy.

In locations where the seismic response can be estimated with a 1D soil model, the horizontal to vertical spectral ratio (HVSR) method can be applied. This ratio gives the proportion of horizontally polarized energy to vertically polarized energy as a function of frequency. The peak in this ratio has been interpreted as the fundamental resonance frequency for the soil column and the amplitude interpreted as the local site effect, $S(f)$, (e.g. Nakamura 1989, 2000):

$$S(f) = \frac{H(f)}{V(f)} \quad (2.2)$$

where $H(f)$ and $V(f)$ are spectra of horizontal and vertical components, respectively. The interpretation that the ratio can be interpreted as the local site effect is based on the assumption that the horizontally polarized energy is dominated by SH-waves. For situations where the subsurface has a high impedance contrast HVSR seems to correctly detect the soil resonance frequency (Bonney-Claudet *et al.*, 2008; Albarello and Lunedei, 2010).

However, it has also been shown that no SH-resonance is necessary to explain HVSR (Fäh *et al.*, 2001). An alternative explanation is that HVSR is related to the ellipticity of Rayleigh waves (e.g., Bonney-Claudet *et al.*, 2006) and the peak in HVSR is mainly controlled by the velocity contrast between bedrock and sediment (Fäh *et al.*, 2003). Theoretically, the wavefield is dominated by surface waves for distances greater than one wavelength from the source. The challenge in interpreting HVSR as the ellipticity of Rayleigh waves is that the recorded wavefield is a combination of Rayleigh and Love surface waves, for both fundamental and higher modes (Lachet and Bard, 1994; Arai and Tokimatsu, 2004, 2005; Fäh *et al.*, 2001; Poggi and Fäh, 2009).

CHAPTER 3

DATA ACQUISITION

The experiments were carried out during June 2009, in or near the St. George and Cedar City urban areas. Figure 3.1 shows the location of the six arrays deployed in this study. The locations were in most cases collocated with permanent strong-motion seismometers and were chosen to characterize representative geologic depositional environments for the region. These geologic environments are as follows: (1) The Cedar Valley, where Cedar City is located, is in the transition zone between the Basin and Range and Colorado Plateau physiographic provinces. The exposed geology of this area includes rocks of Paleozoic, Mesozoic, and Cenozoic age (Eisinger, 1998). The mapped sediments of interest are composed of Tertiary conglomerates with interbedded basalt flows and Quaternary piedmont-slope alluvium (Rowley *et al.*, 2006). (2) The St. George basin, encompassing the St. George–Hurricane metropolitan area. The stratigraphic column of the basin consists of a thick sequence of sedimentary rock formations and thinner unconsolidated deposits (i.e. shallow bedrock) that range in age from Paleozoic to latest Holocene (Lund *et al.*, 2008). The arrays targeted sites with exposed rock and sites with alluvial-stream deposits and alluvial plus eolian deposits (Higgins and Willis, 1995). The location of the seismic arrays we deployed and the geologic environment at each array are summarized in Table 3.1.

At each site we deployed an array of four seismic sensors. The sensors used were three-component nanometrics Trillium-120 broadband seismometers connected to Geotech Smart-24R recorders. At each array location, the sensors were deployed in an equilateral triangular configuration (Asten and Boore, 2005; Stephenson, *et al.*, 2009) as Okada (2001) demonstrated that SPAC coefficients obtained from a

triangular array with four stations is not substantially different from that obtained from a circular array with more sensors. The array geometry is shown in Figure 3.2. In choosing site locations, the goal was to locate the sensors on either concrete or asphalt. The primary reason for this is to minimize possible shifting of the sensors during recording. In a typical design, sensors in the 10 m radius array were placed in a common parking lot, sensors in the 30 m and 90 m arrays were mostly placed along two perpendicular sidewalks or in adjacent parking lots. At sites where it was impossible to find appropriate sidewalks or parking lots, sensors were placed on paving stones laid onto grass. At each site, the array was set up with three different distances between the center sensor (see Figure 3.2) and outer sensors. The distances used were approximately 10, 30, and 90 m. For each configuration we collected roughly 30 minutes of data sampled at 100 Hz.

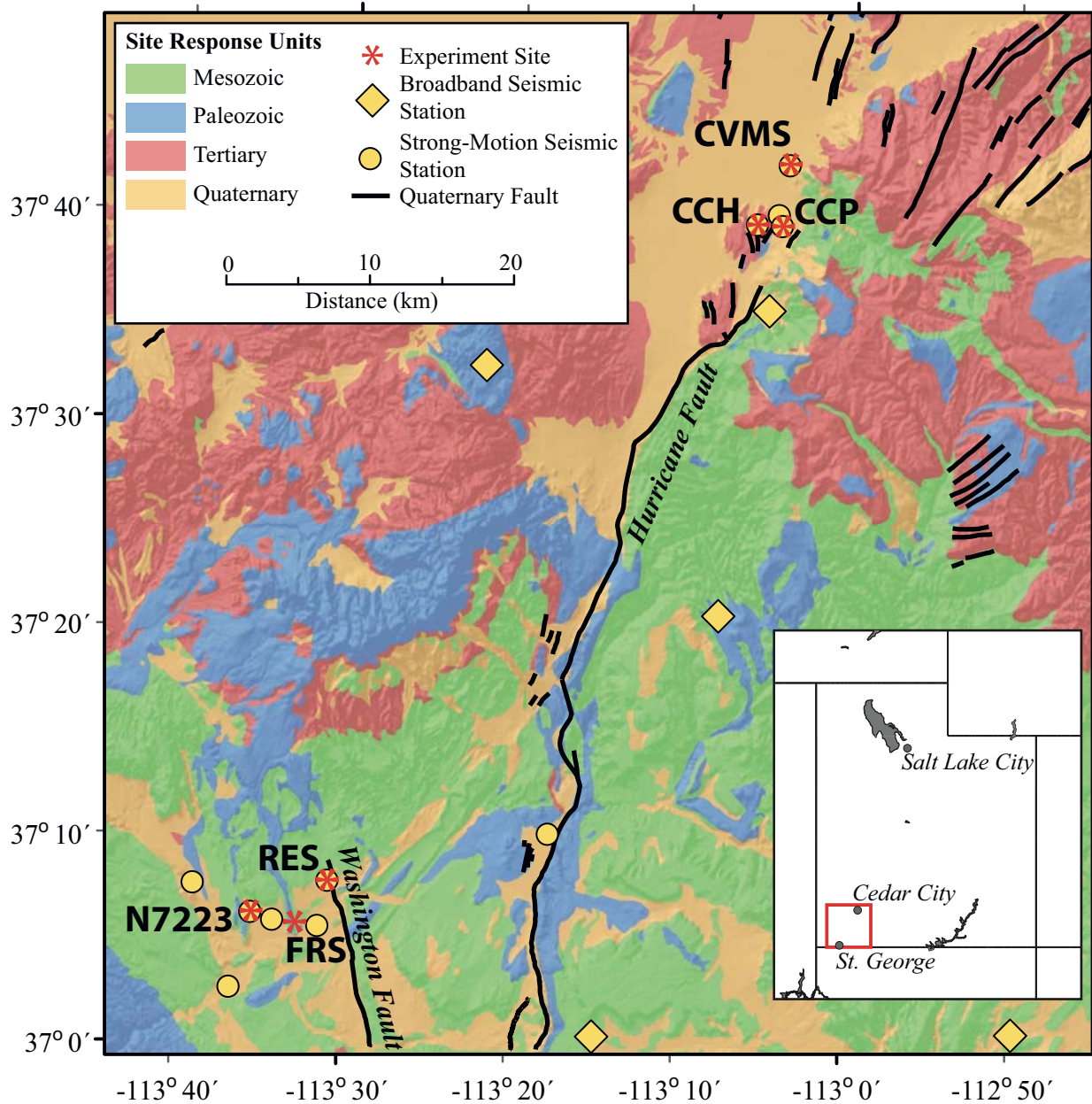


Figure 3.1. Geologic and site location map for the study area. The overall study region is shown in the inset in the lower right corner. The primary study area encompasses the cities of Cedar City and St. George, Utah, as outlined by the red box. In the main panel the colors indicate the age of the geologic units. Quaternary faults are shown as solid lines and the two most prominent faults in the area are labeled (the Hurricane and Washington Faults). The locations of the seismic arrays we deployed in this study are shown as red bursts and seismic stations as either yellow circles (strong-motion) or diamonds (broadband).

Table 3.1. Site location and geologic description

Site		Latitude	Longitude	Geologic Description
CCH	Cedar City Church	37.66°	-113.09°	Tertiary conglomerate with interbedded basalt flows ¹
CCP	Cedar City High School	37.66°	-113.07°	Quaternary piedmont-slope alluvium silt, sand, and gravel ¹
CVMS	Canyon View Middle School	37.71°	-113.06°	Quaternary piedmont-slope alluvium silt, sand, and gravel ¹
FRS	Fossil Track Intermediate School	37.10°	-113.54°	Shallow Jurassic Moenave Formations siltstone and sandstone ²
N7223	Dixie State College	37.10°	-113.57°	Quaternary mixed alluvial and eolian deposits clay to sand ²
RES	Riverside Elementary School	37.10°	-113.52°	Quaternary alluvial-stream deposits clay to small gravel ²
¹ Rowley <i>et al.</i> , 2006 ² Higgins and Willis, 1995				

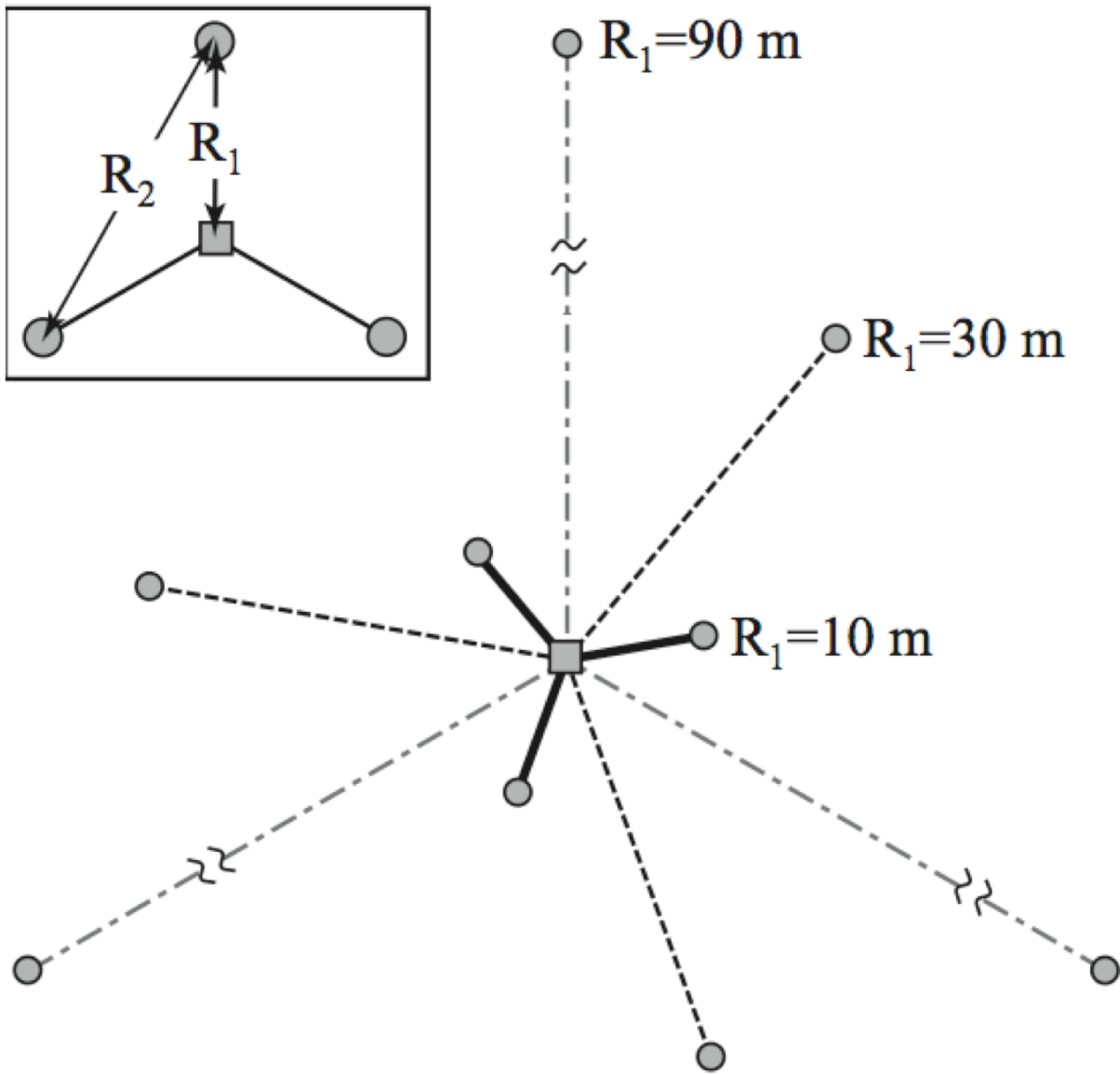


Figure 3.2. Array geometry of the microtremor survey. Three of the four sensors were placed at the vertexes of an equilateral triangle with the fourth sensor placed at the center. The sensors are deployed three times at each site with a different distance between the center sensor and the outer sensors in each case. Distance between the station at the center and at each vertex was set to 10 m, 30 m and 90 m. Analysis between sensors can be carried out in two configurations (upper left panel): (1) between the center sensor and each outer sensor (radius = R_1), (2) between each of the outer sensors (radius = R_2).

CHAPTER 4

DATA PROCESSING

For each site our goal is to determine the S-wave velocity model in the shallow subsurface. We do this by forward modeling using the MMSPAC technique and then refine this model by analysis of the HVSR data; ultimately comparing the resulting models to dispersion curves determined using traditional SPAC analysis. In order to carry out this analysis we first process our data in the following three stages: (1) we calculate the coherency between sensors, (2) we calculate the HVSR, and (3) we calculate the phase velocity dispersion curves. We outline the basic steps involved in each processing step in this section and describe the forward modeling effort in the next section.

All data were pre-processed by first tapering the 30-minute long files and then bandpass filtering between 0.1 and 20 Hz using a Butterworth filter. Our first step was to calculate the coherency for each pair of stations collected at each array dimension. Coherency is defined in the frequency domain as:

$$c(f) = \frac{F_1 \times F_2^*}{\sqrt{(F_1 \times F_1^*) \times (F_2 \times F_2^*)}} \quad (4.1)$$

where, $c(f)$ is the frequency dependent coherency, f is frequency, F_1 and F_2 are the Fourier transforms of the time series of the stations pairs, and F_1^* and F_2^* are the complex conjugate of F_1 and F_2 respectively. The \times operator represents multiplication.

The azimuthally averaged coherency curve was then found by averaging each coherency curve calculated with the same interstation spacing at each site. For example, at a single site we process the data as follows: (1) we calculate the

coherency as defined in equation 4.1 for each of our six interstation spacings (10 m, 30 m, and 90 m in the R1 configuration and 17 m, 51 m, and 155 m in the R2 configuration - Figure 3.2). In the R1 configuration, coherency is calculated between the center sensor and each of the outer sensors. In the R2 configuration, coherency is calculated between pairs of outer sensors. Thus, at each site we have six interstation spacings \times 3 sensor pairs, giving a total of 18 individual coherency curves. (2) We next average the three coherency curves at each interstation spacing giving us a single curve at that spacing. This step is repeated for each distance, resulting in 6 azimuthally averaged coherency curves at each station for the six possible radii.

Results for sites CVMS, N7223, and RES are shown in Figure 4.1. Results for all sites at all distances are included in the appendix. In each panel of Figure 4.1, the solid black line shows the Real part of the azimuthally averaged coherency, whereas the imaginary part is shown with the light gray line. Large deviations from zero of the imaginary part of the coherency curve are indicative of the assumptions behind SPAC failing. Here we do not see significant departure from zero of the imaginary portion. The real part of the coherency curves show two major trends: (1) at larger interstation spacing we see more oscillations in the coherency curve, and (2) at the lowest frequencies the coherency often tends to drop towards zero. The larger number of oscillations at greater interstation spacing is expected and is best understood by referring back to equation 2.1. The Bessel function is a function of both frequency and distance (and can be plotted either way). With increasing distances, we expand the domain of the Bessel function and see a longer window of the oscillating Bessel function. However, the coherency should approach unity at the lowest frequency. The loss of coherency at the lowest frequencies has been noted in previous studies for similar array geometries (e.g., Stephenson *et al.*, 2009).

The horizontal to vertical spectral ratio (HVSR) is determined for the entire 30 minute data window by calculating the geometric mean of the HVSR determined for consecutive 20-second long windows. Before computing the spectrum of each window, the mean is removed and a 5% Hanning taper is applied. The spectrum

of each component is smoothed separately using a ± 2 -point running average. The ratio for each window is determined by dividing the average of the spectrum from the two horizontal components by the spectrum of the vertical component. The HVSR was determined at all four sensors in the array and at all three array dimensions.

The thin gray lines in Figure 4.2 show HVSR for each site at three interstation spacings of 10, 30, and 90 m. The HVSR curves show a high degree of similarity for the different interstation spacings, except for the 90 m distance at station N7223 (not shown in figure). In particular, the peak amplitude is similar in each case. This is important because forward modeling efforts of ellipticity, described below, will focus on matching the amplitude, position, and shape of these HVSR curves.

Dispersion curves were obtained by correlating the azimuthally averaged coherency curves to a theoretical Bessel function (see equation 2.1). This is done at each site for each interstation spacing. A single phase velocity dispersion curve is then obtained by combining the phase velocity measurements determined from each interstation spacing. For each of the six interstation spacings, we calculate the phase velocity from the first maximum to the first minimum in coherency. Because the first maximum, first minimum, and first zero-crossing point are at different frequencies, we get six phase velocity curves distributed at different frequencies. In order to combine them into a single dispersion curve, we select the part around the first zero-crossing in the individual curves, which we believe to be most reliable. After cutting out these subsections there are small gaps in frequency so we interpolate between these gaps to produce a continuous curve. Results for each site are shown in Figure 4.3. The heavy black line shows the calculated dispersion curves. The different sites show robust dispersion curves in different frequency bands as is expected from the differing site geology and our method described above. Figure 4.4 shows observed coherencies versus theoretical coherencies determined using the modified MMSPAC method. The results of the HVSR calculations are shown in Figure 4.5.

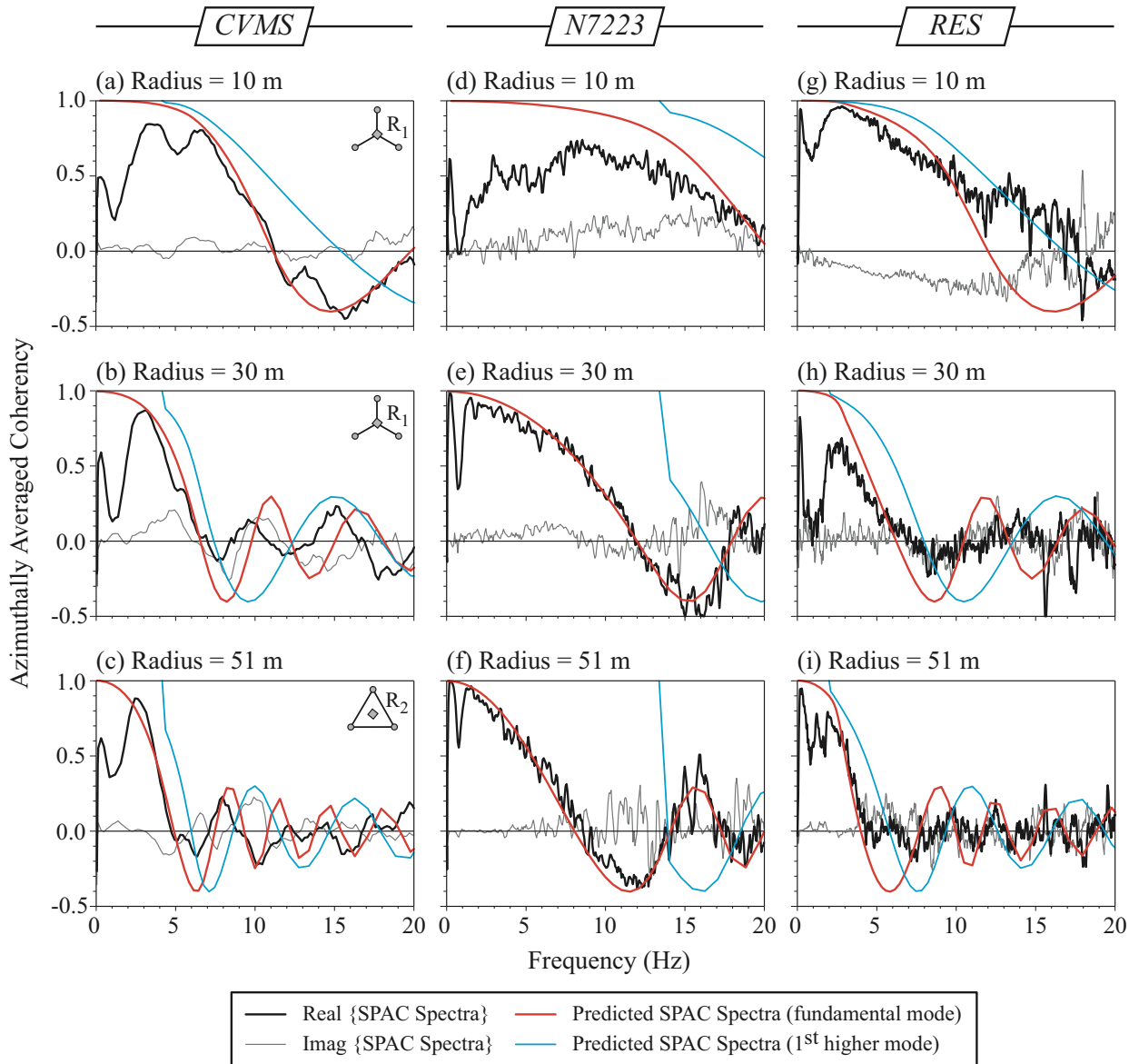


Figure 4.1. Observed coherencies versus theoretical coherencies determined using the method of MMSPAC. Black thick lines are the observed coherency curves, red lines are the theoretical coherency curves for the fundamental mode, light blue lines are the theoretical coherency curves for the first higher mode. The gray thin line is the imaginary part of the observed coherency. Each column represents measurements at a single site (CVMS, N7223, or RES) at three different distances. The top two rows show measurements in R1 (see Figure 3.2) and the bottom row shows measurements in R2.

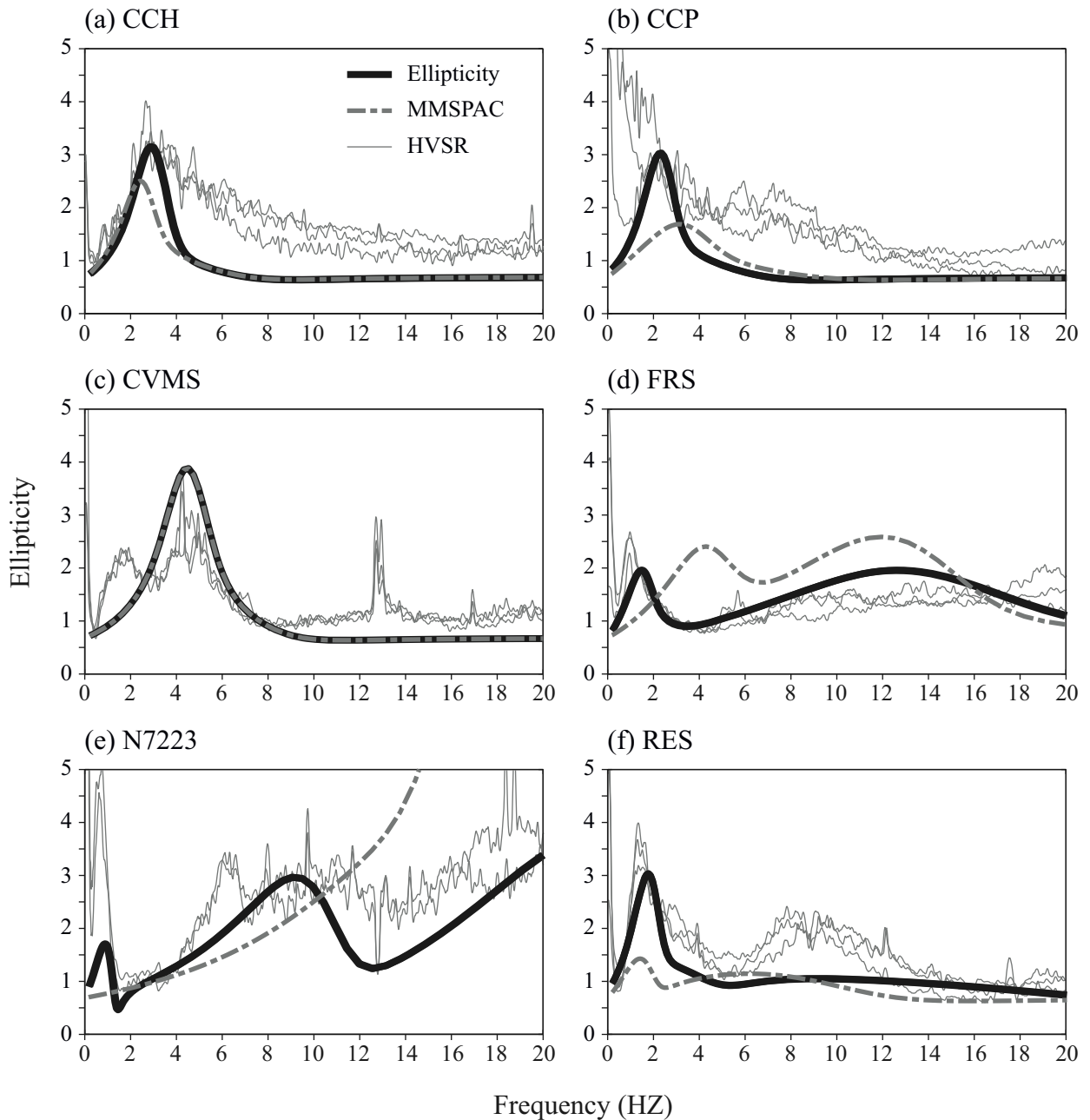


Figure 4.2. Horizontal to vertical spectral ratios (HVSr) compared to theoretical ellipticity curves predicted for two models. Gray thin line is HVSr of data from a station at 10 m, 30 m, and 90 m distances. Gray dashed line is predicted ellipticity for the models determined using MMSPAC, black thick line is predicted ellipticity for the models modified to best fit the HVSr data.

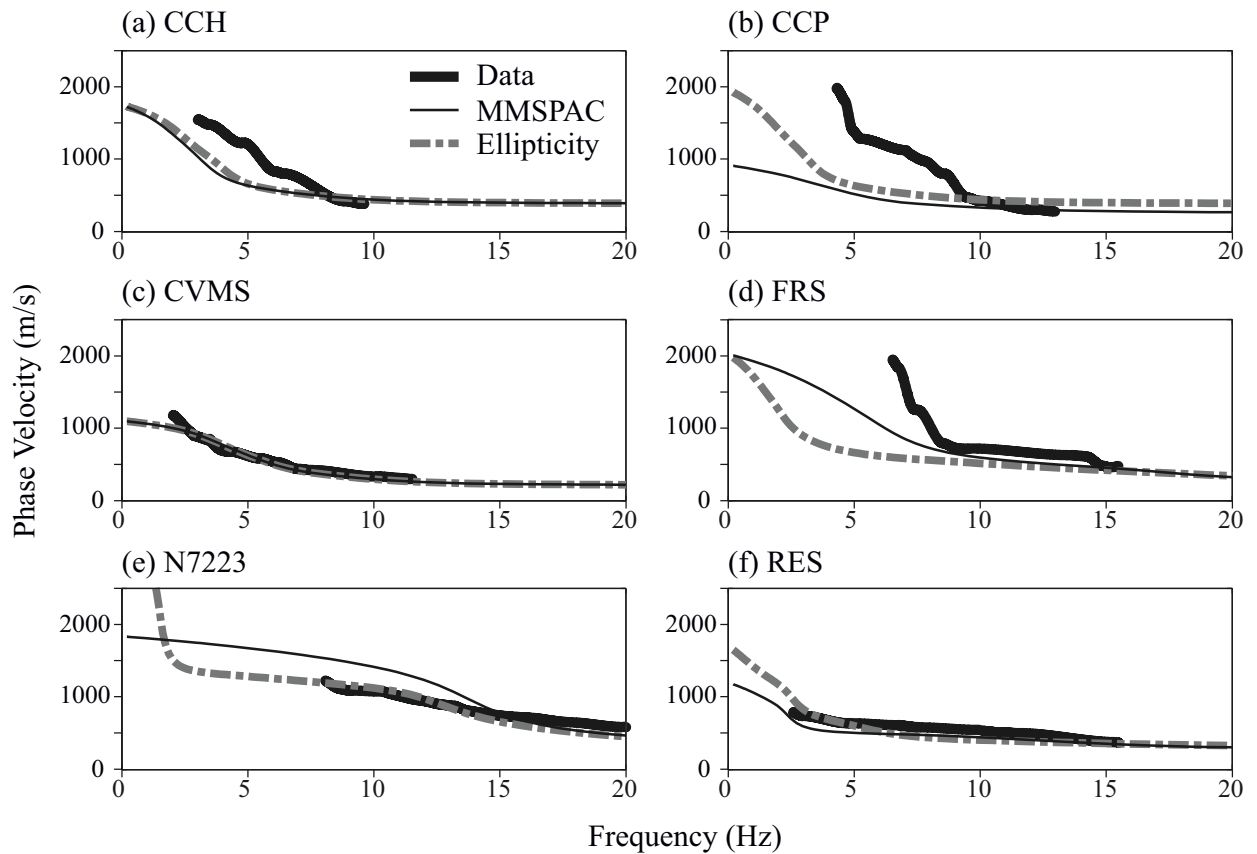


Figure 4.3. Phase velocity dispersion curves of data and models. Black thick line is phase velocity calculated using the traditional SPAC method, gray dashed lines are phase velocity dispersion curves for models determined using MMSPAC, black thin lines are phase velocity dispersion curves for models modified to fit the HVSR data.

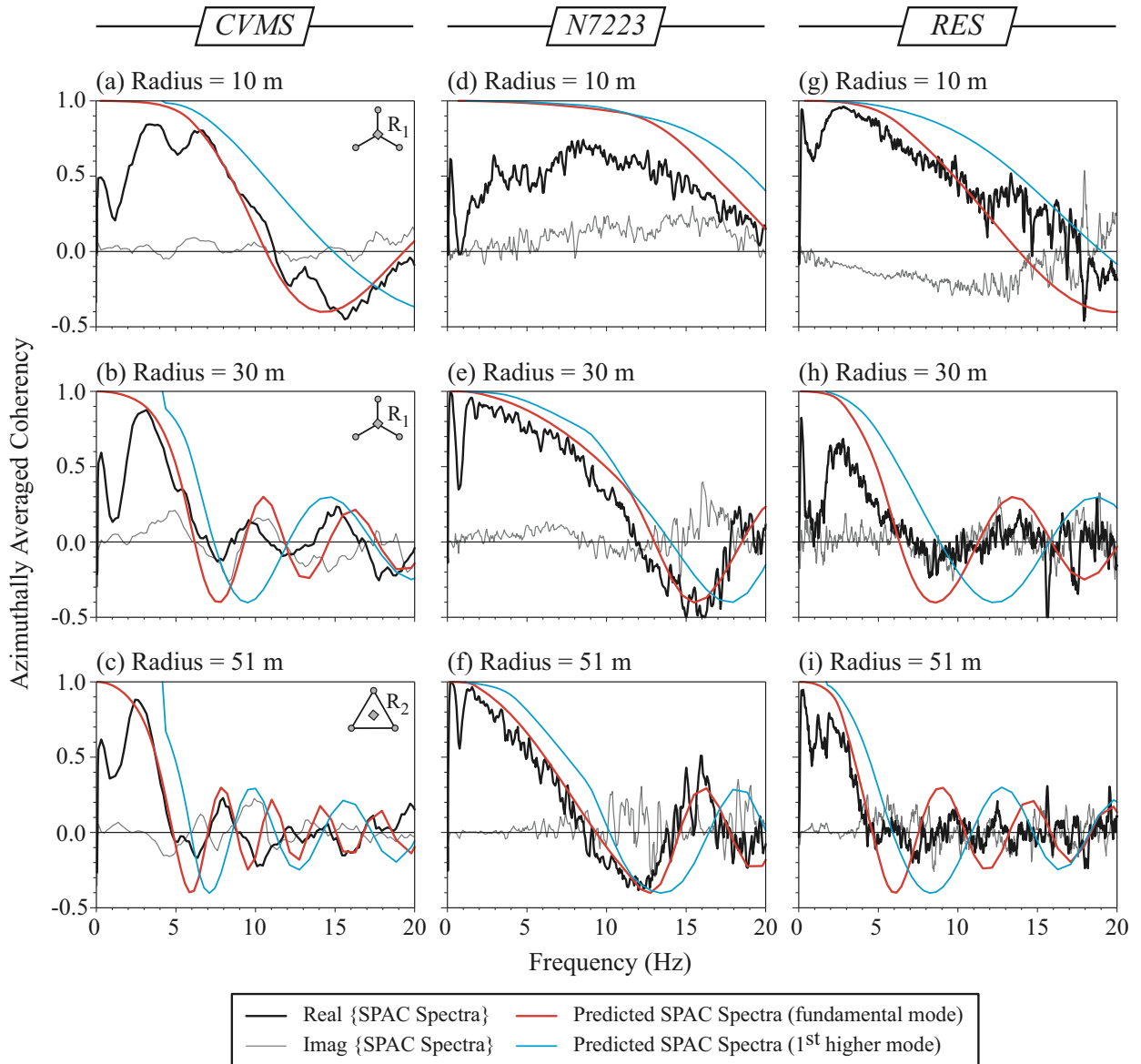


Figure 4.4. Observed coherencies versus theoretical coherencies determined using the modified MMSPAC models. Black thick lines are the observed coherency curves, red lines are the theoretical coherency curves for the fundamental mode, light blue lines are the theoretical coherency curves for the first higher mode. The gray thin line is the imaginary part of the observed coherency. Each column represents measurements at a single site (CVMS, N7223, or RES) at three different distances. The top two rows show measurements in a R1 configuration (see Figure 3.2) and the bottom row shows measurements in a R2 configuration.

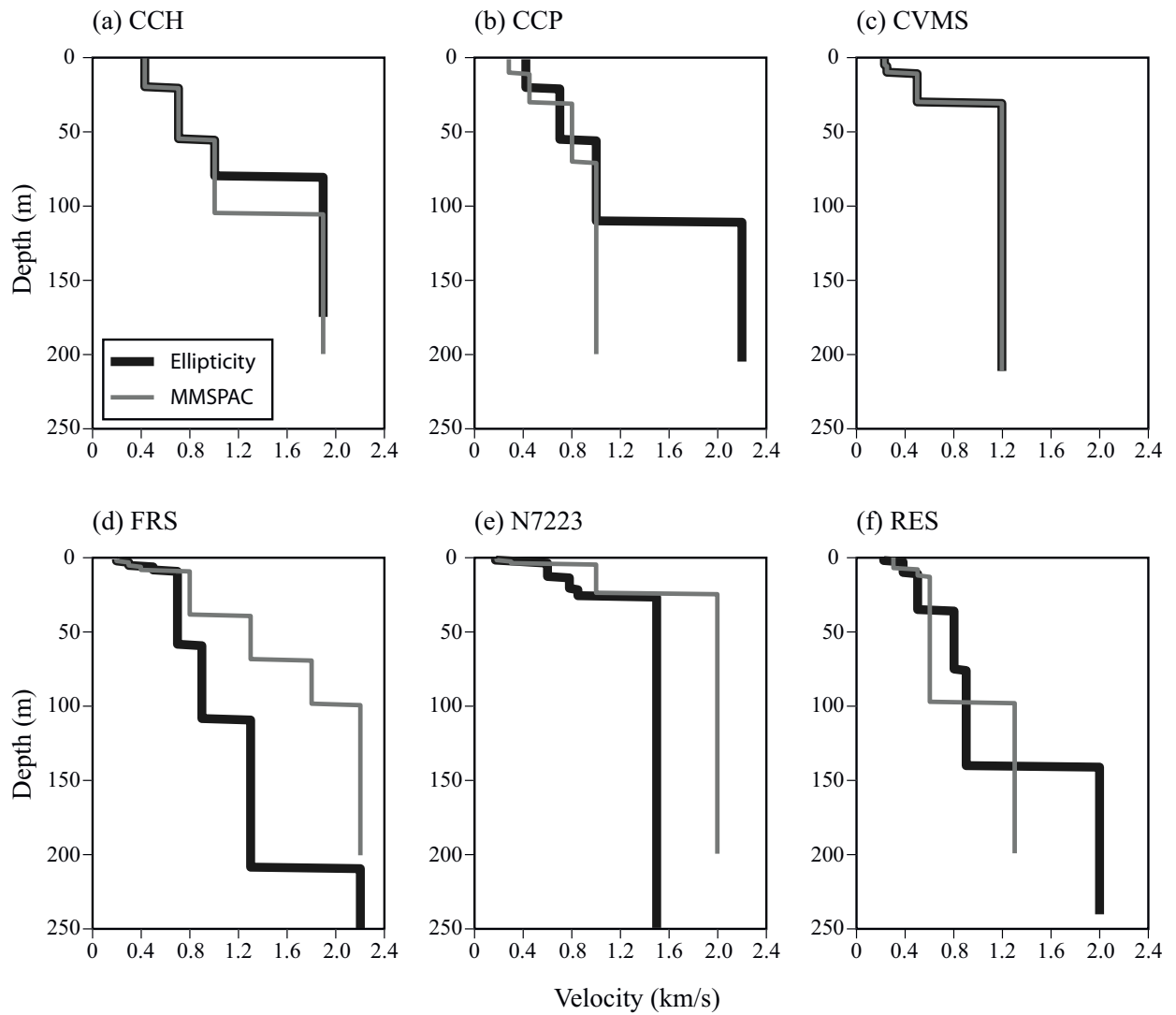


Figure 4.5. Shear-wave velocity models. Models for each of the six sites are shown for the two techniques used in this study. Gray lines show models determined using MMSPEC and black lines show models modified to have the ellipticity fit the HVSR. In each case the S-wave velocity models are truncated at the lowest resolvable depth.

CHAPTER 5

FORWARD MODELING S-WAVE VELOCITY STRUCTURE

We began the modeling process using MMSPAC. Compared to traditional SPAC, MMSPAC has several advantages: (1) it avoids possible errors introduced by inverting the phase velocity dispersion curves; (2) the reliable part of the coherencies is not limited to the range between the first maximum and first minimum; and (3) it is also possible to fit not just the fundamental, but the higher mode Rayleigh waves (Asten, 2006). Initial models, including layer thickness, P- and S-wave velocities, and density, were determined using geologic information provided for each site (Bill Lund, personal communication, 2009). The modeling process involves (1) specifying an initial elastic model and (2) computing the theoretical coherency curves for the fundamental and first two overtones of the Rayleigh wave modes. By iteratively adjusting the model parameters, we optimized the fit between the observed coherencies and the theoretical coherencies, at all 6 interstation spacings (10 m, 17 m, 30 m, 51 m, 90 m, and 155 m) simultaneously. In adjusting the model parameters, thickness and S-wave velocity had the greatest effect on the shape of the coherencies. Figure 4.1 shows examples of the degree to which we were able to fit the data using MMSPAC for stations CVMS, N7223, RES. (See the appendix for all stations.) We will discuss these model fits with respect to each site in the Results section.

Because of the trade-off between S-wave velocity and layer thickness when modeling and sensitivity of MMSPAC to the shallow structure, we use the HVSR data to better constrain the velocity models. In our analysis, we interpret that the microtremors are dominated by Rayleigh waves. We thus model the HVSR data as

being representative of the Rayleigh wave ellipticity. We use the Geopsy software package to generate the theoretical ellipticity curves for the models determined using MMSPAC. The dashed lines in Figure 4.2 show the comparisons with the HVSR data. With the exception of the array at CVMS, the peak in the predicted ellipticity is mismatched compared to the data.

Because of the misfit between peak predicted ellipticity and the peak in the HVSR data we next sought to improve upon the models. In the next stage of modeling, the velocity models determined using MMSPAC were iteratively adjusted to provide a better fit between predicted ellipticity and the HVSR curves. The solid lines in Figure 4.2 show these improved fits. In most cases, the primary change is to the deeper part of the model at the deepest velocity contrast (Figure 4.5). To confirm that these revised models still match the coherency curves, we calculated new coherency curves with MMSPAC. The new coherency curves are shown in Figure 4.4. When compared with our initial coherency curves (Figure 4.1) we see little change thus indicating the additional modeling does not significantly degrade the coherency fit.

As a final comparison of the models, we used the Geopsy software to generate fundamental mode Rayleigh wave dispersion curves for the model determined with MMSPAC and the refined model using the HVSR data (Figure 4.3). With the exception of the array at N7223 and FRS, the dispersion curves for the two models are in agreement, especially for frequencies greater than 5 Hz. We discuss how these theoretical dispersion curves compare with data in the next section.

CHAPTER 6

RESULTS

Figure 4.5 shows the final models for the six sites. In each case, we present the model determined using MMSPAC and the model optimized by modifying the MMSPAC model to fit the HVSR data using ellipticity curves. As expected for most cases the major differences in the models are in the deeper structure since the peak in HVSR is mainly controlled by the velocity contrast between bedrock and sediment (Fäh *et al.*, 2003). To assess the models, we also compare the results to the dispersion curves determined using traditional SPAC (Figure 4.3). Important aspects in using these models for seismic hazard analysis include the average shear velocity in the upper 30 meters (V_s30) and the general shape of the profiles including depth to bedrock. The final models are summarized in Table 6.1.

Sites in the Cedar Valley include CVMS, CCP, and CCH. Both CVMS and CCP are located in Cedar City over what is thought to be deep basin fill. Based on previous geologic studies (there are no other direct velocity measurements at these sites), it was expected that the two locations would have similar profiles and the profile would show a gradual increase in velocity with depth. The best modeled site is CVMS. Instead of a gradual increase in velocity we find a simple step in V_s at 30 m. Here the model determined using MMSPAC also predicts an ellipticity curve that matches the HVSR curve. This model also provides a nearly perfect match to the dispersion curve for frequencies between 2 and 12 Hz. The model determined using MMSPAC for CCP is consistent with what was expected (namely a gradual increase in velocity with depth). However, the peak in the HVSR argues for a deeper high velocity unit, as shown in the revised model. We can not resolve the discrepancy between these two models, however it should be noted that neither

model fits the coherency curves exceptionally well (see the appendix). The HVSR data for this site at the different distances also shows the largest disagreement, and a well defined peak is not as apparent as at other sites. However, the phase velocity data at CCP suggest a rapid increase in velocity at the lowest frequencies which is more consistent with a velocity jump than a gradual increase. Given the differences in the data between the two sites and how well fit all the data for CVMS are, we argue that the geology is indeed different between the locations. We are at a loss to interpret the shallow velocity increase at CVMS in context with what is expected from the previous geologic studies. However, this velocity increase is well modeled and appears to be real.

The third site located in the Cedar Valley is CCH. The initial modeling using MMSPAC indicated a depth to a high velocity discontinuity at 100 m. Yet, to fit the peak in HVSR located between 3-4 Hz, the deepest interface was decreased from 100 to 80 m. Both models suggest similar phase velocity curves which agree in shape with that from the data. Nonetheless, the data suggest higher phase velocities at the shortest frequencies which could indicate we are underestimating the velocity jump in the deepest layers. Unlike the other two Cedar City locations, this array was located outside of the basin on a nearby hill. The geology at the site is a Tertiary conglomerate with interbedded basalt flows (Rowley *et al.*, 2006). Because of the nature of the geology, the deepest interface might be a bedrock contact. Alternatively this contact might be the top of a basalt layer. We are unable to distinguish between the two interpretations.

The three sites located in the St. George basin (FRS, N7223, and RES) have very different depositional environments to those in Cedar City and to each other. Overall, we expect shallow bedrock in the St. George area. A potential obstacle to obtaining deep S-wave velocity profiles in the St. George area is the presence of caliche. Caliche, otherwise known as hardpan, is calcareous material of secondary origin that typically accumulates in the shallow subsurface of soils in arid and semiarid climates (Bates and Jackson, 1987). This material will have high seismic velocities making it difficult to see deeper lower velocity material.

FRS was selected in order to characterize a rock site. This location is mapped as the Jurassic Moenave Formation - a siltstone/sandstone formation (Higgins and Willis, 1995). For this location the MMSPAC model was determined by fitting the higher modes. The predicted ellipticity for the MMSPAC model does not agree with the HVSR data at all. To fit HVSR we had to lower the velocities over the entire profile. However, the higher velocities from the MMSPAC model better match the dispersion data. In addition, the higher velocities are more consistent with this being a rock site.

In the other two St. George sites, the surface geology is mapped as Quaternary alluvial deposits (Table 3.1). At the location of N7223 both MMSPAC and ellipticity modeling suggest strong velocity increases at depths less than 10 m and between 24 to 30 m. To fit the HVSR data, it was necessary to decrease the velocity increase at 30 m from 2.0 km/s to 1.5 km/s and add velocity increase to 3.5 km/s at 400 m (deeper velocity increase not shown in Figure 4.5). The phase velocity curve calculated from the HVSR data better fits the dispersion curve for the frequency range where phase velocities could be determined and fits the general trend of the dispersion curve at the lower frequencies. The rapid increase in velocity at 3 to 4 m is consistent a caliche layer. The velocities are too high for the mapped alluvium or eolian deposits (Table 3.1).

MMSPAC modeling at RES suggested a velocity interface at 98 m. To match the HVSR data, this interface was increased to a depth of 140 m and a new layer at roughly 40 m was also introduced. These model adjustments caused the ellipticity peak to shift to higher frequencies and a higher amplitude. The modified model predicts a dispersion curve that shows slightly better agreement with the dispersion data than the MMSPAC model. Both models are generally consistent with what would be expected (a gradual increase in velocity with depth) for an alluvial layer over bedrock.

Table 6.1. Results

MMSPAC Model					Ellipticity Model			
Site	¹ V _s 30 (m/s)	Bedrock Depth (m)	V _s Jump (m/s)	NEHRP Code	¹ V _s 30 (m/s)	Bedrock Depth (m)	V _s Jump (m/s)	NEHRP Code
CCH	485	105	1000- 9000	C	485	80	1000- 1900	C
CCP	374	60	800- 1000	C	485	120	1000- 1200	C
CVMS	367	30	500- 1200	C	367	30	500- 1200	C
FRS	545	*	1800- 2200	C	522	*	1300- 2200	C
N7223	736	24	1000- 2000	C	529	30	850- 1300	C
RES	462	98	600- 1300	C	413	141	900- 2000	C
¹ Park <i>et al.</i> , 1998								
* Bedrock exposed at surface								

CHAPTER 7

CONCLUSIONS

In Figure 4.5 we showed two sets of models, one set were modeled from MMSPAC by fitting theoretical and observed coherency curves, the other set are the models after being adjusted to make the ellipticity fit the HVSR curves. For all sites except FRS, we consider the models refined using HVSR to provide the best fit to the data. All models except that for CVMS seem reasonable given what is known of the geology. At CVMS the models are well constrained by the data. Given the large discrepancy in the models determined in this study with what is known about the geology, this location should be the target of additional studies.

Importantly for seismic hazard analysis the average shear-wave velocity in the upper 30 m (V_s30) is between 360 and 760 m/s for all six sites. V_s30 was calculated using the methodology of Park (Park *et al.*, 1998). This is the velocity range corresponding to NEHRP site class unit C. Little strong-ground motion amplification is expected for average shear velocities in this range (Borcherdt, 1994).

APPENDIX

SUPPLEMENTAL FIGURES

Supplemental Figures A.1 - A.6 show Observed coherencies versus theoretical coherencies determined using MMSPAC at all six sites at all interstation spacings. Black thick lines are the observed coherency curves, red lines are the theoretical coherency curves for the fundamental mode, light blue lines are the theoretical coherency curves for the first higher mode. The gray thin line is the imaginary part of the observed coherency.

Supplemental Figures A.7. - A.12 show Observed coherencies versus theoretical coherencies determined using modified MMSPAC models at all six sites at all interstation spacings. Black thick lines are the observed coherency curves, red lines are the theoretical coherency curves for the fundamental mode, light blue lines are the theoretical coherency curves for the first higher mode. The gray thin line is the imaginary part of the observed coherency.

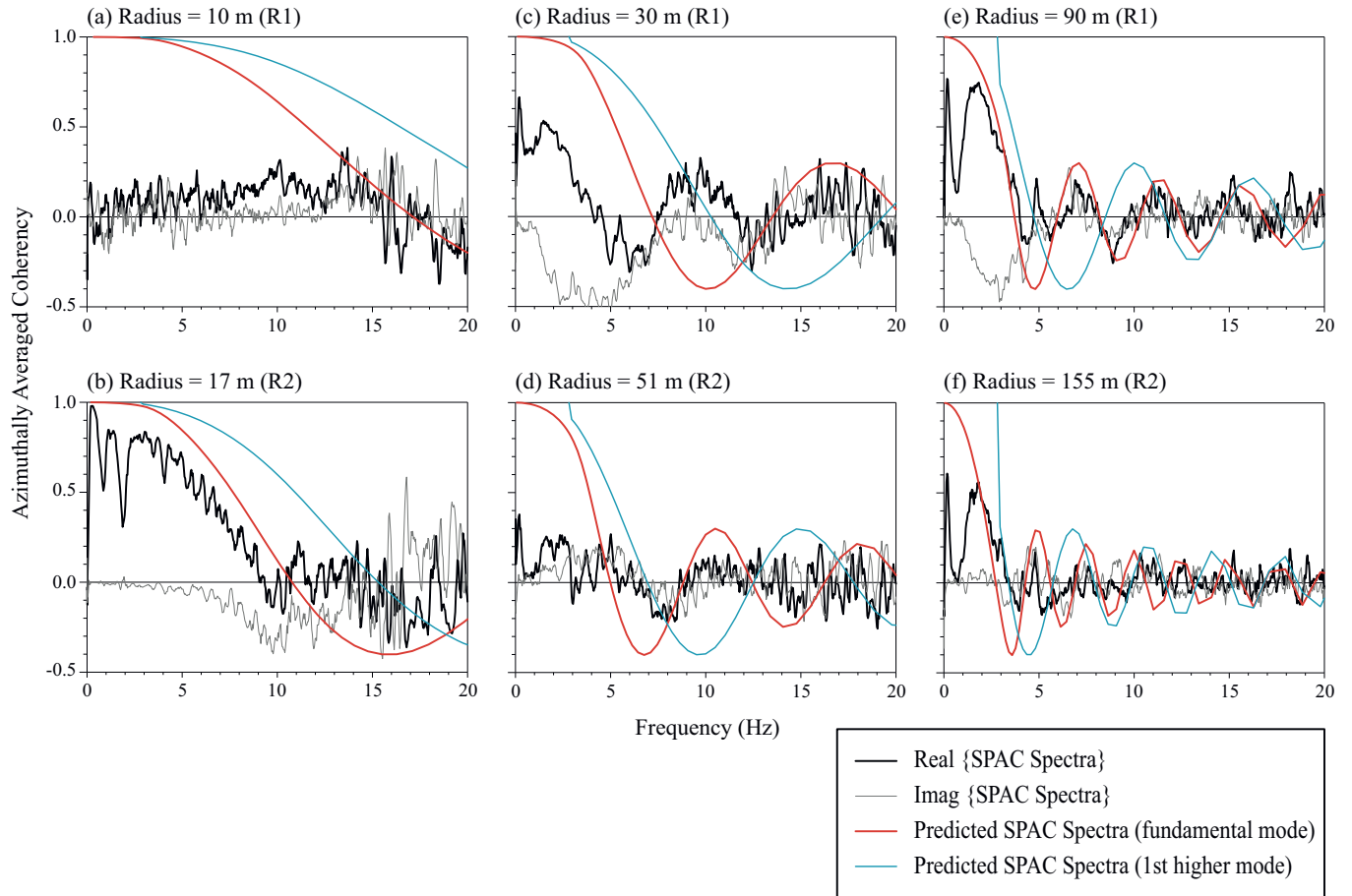


Figure A.1. *Site CCH*

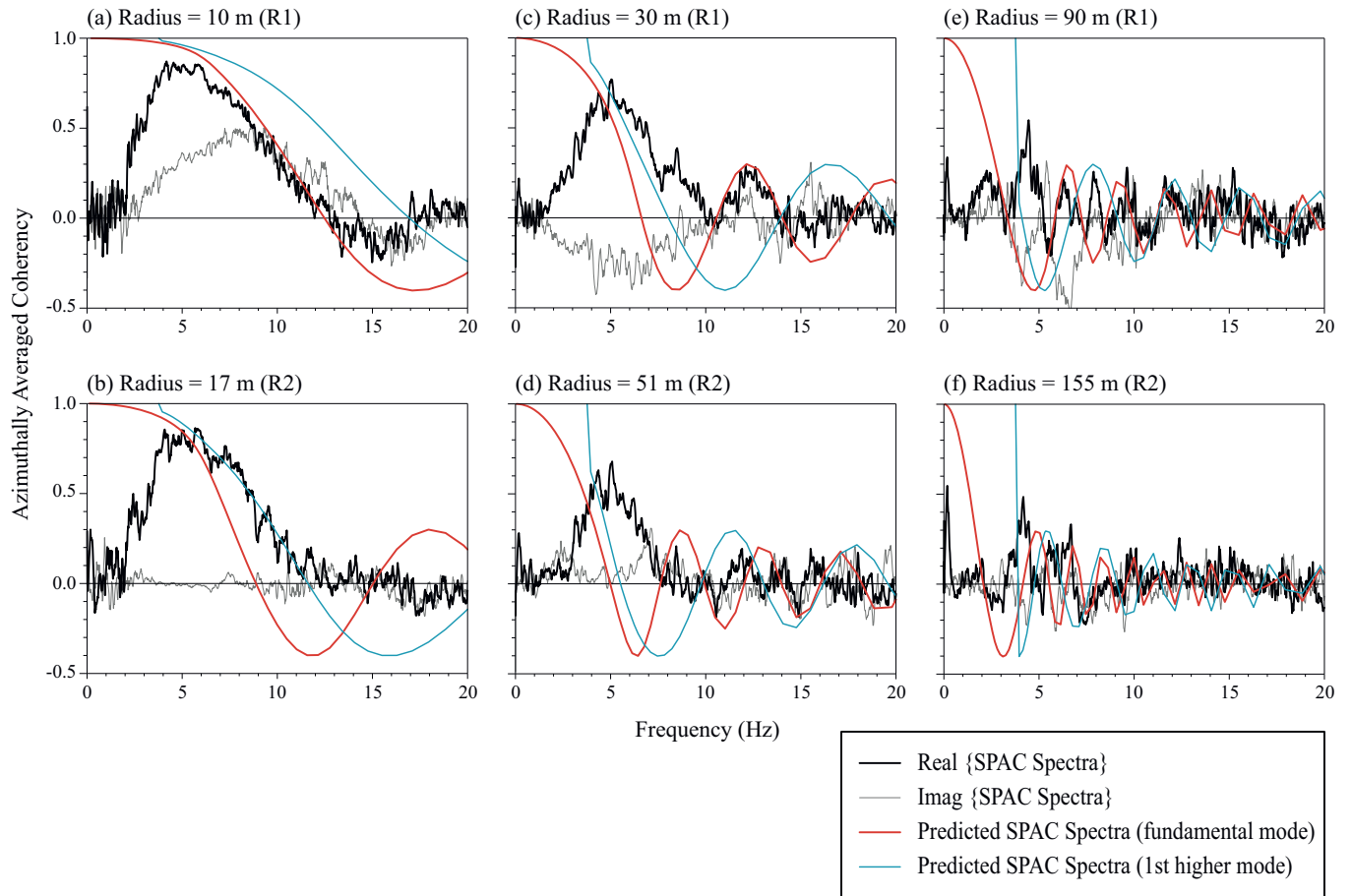


Figure A.2. *Site CCP*

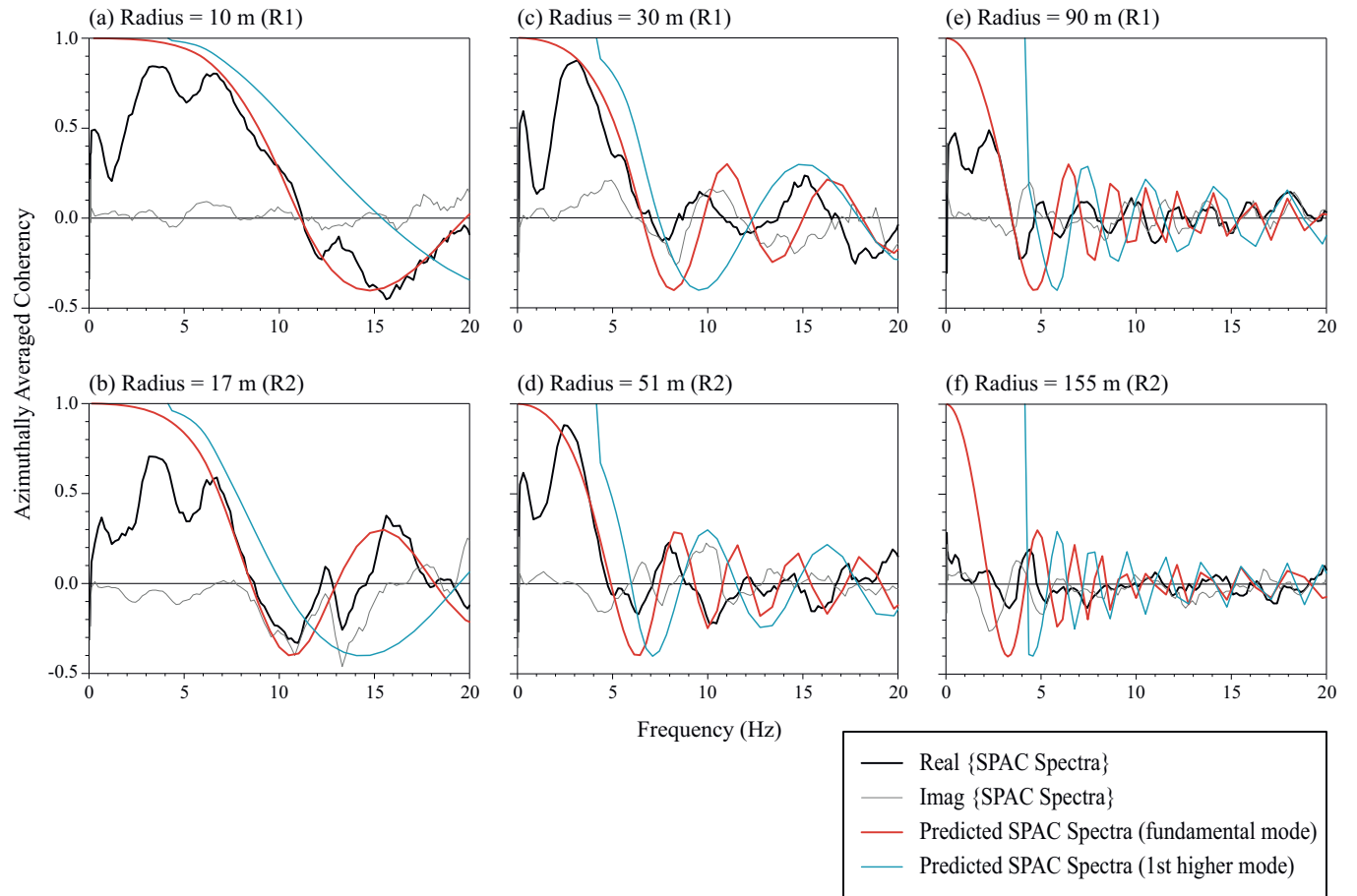


Figure A.3. *Site CVMS*

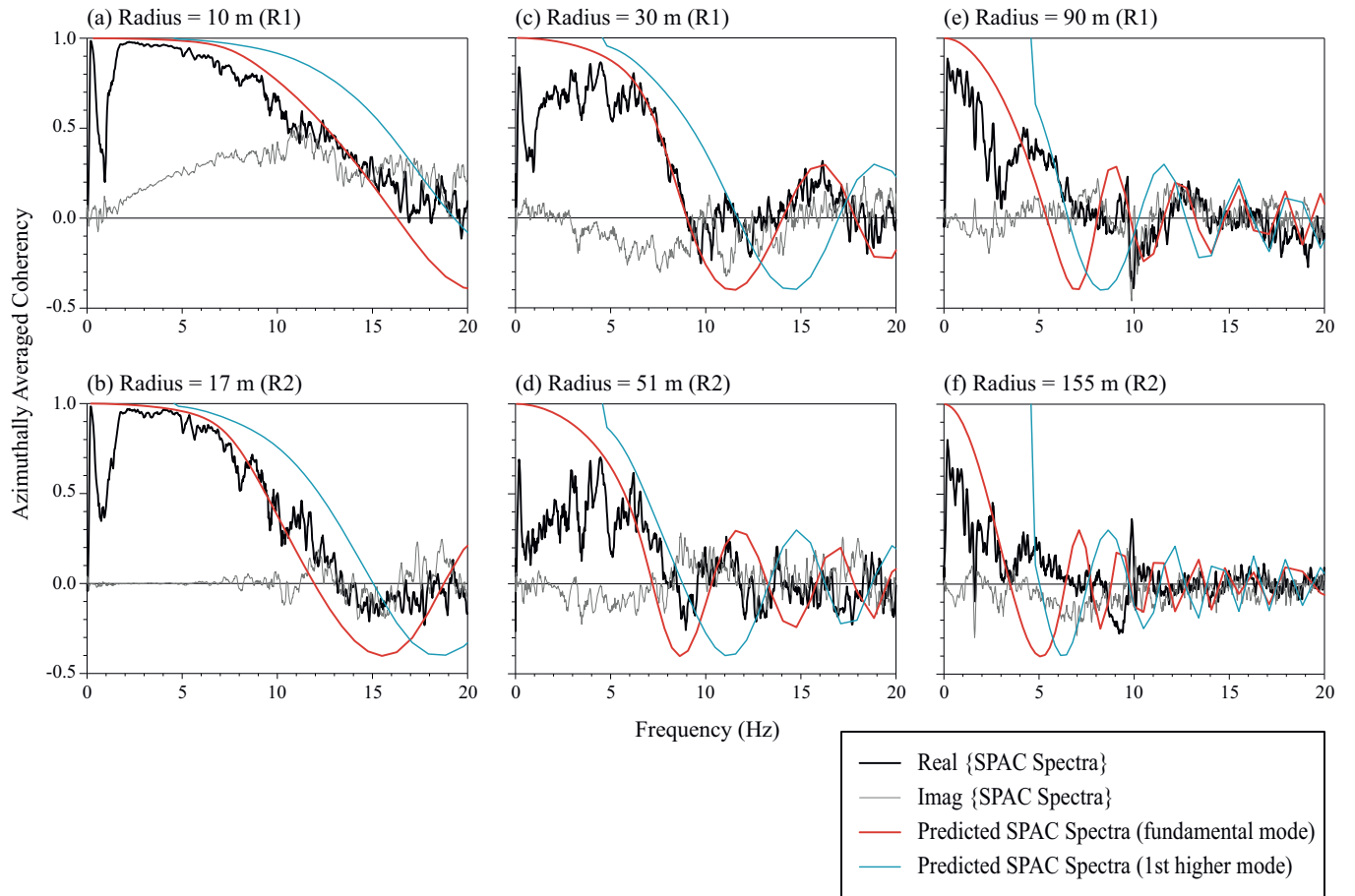


Figure A.4. *Site FRS*

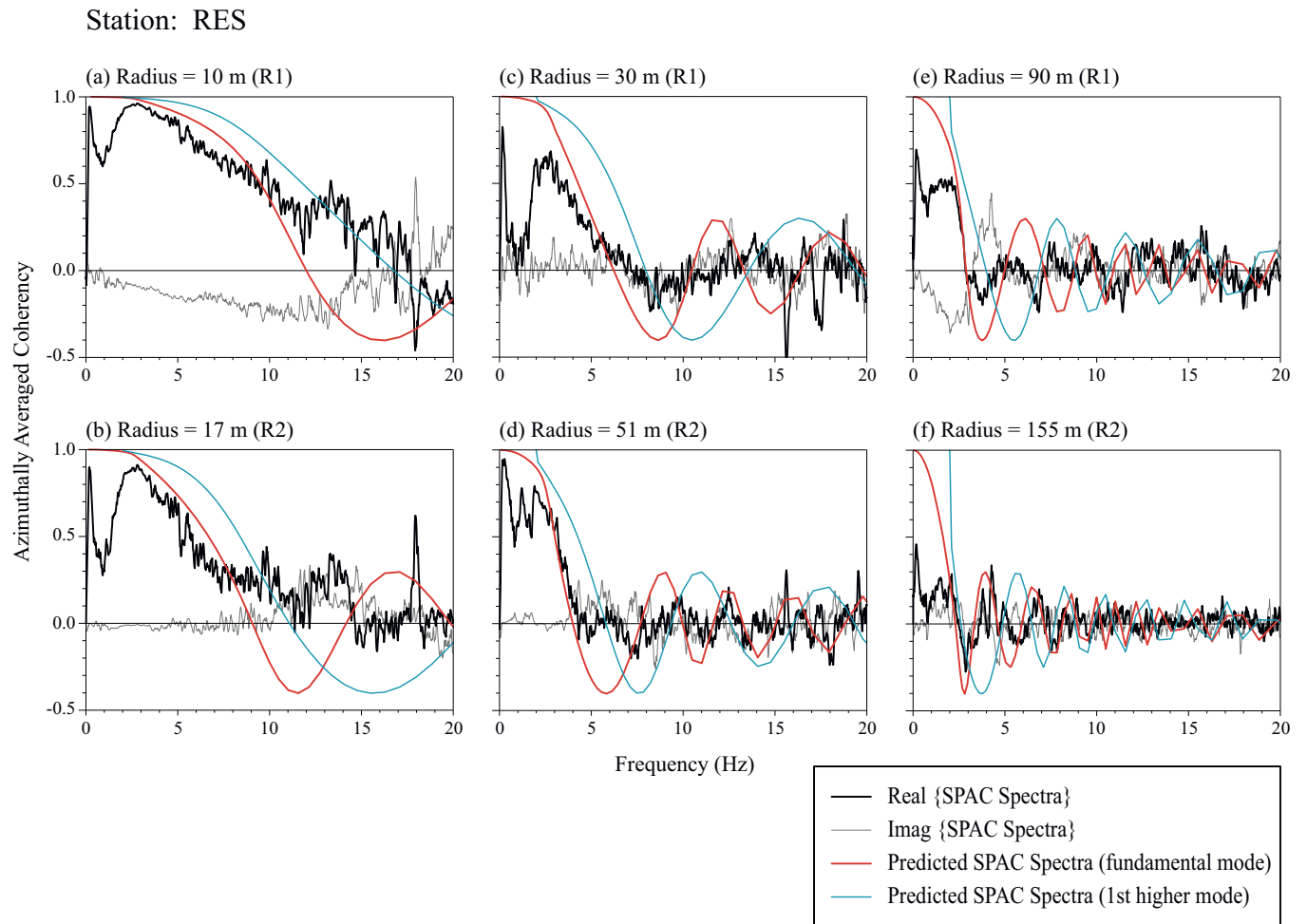


Figure A.5. Site RES

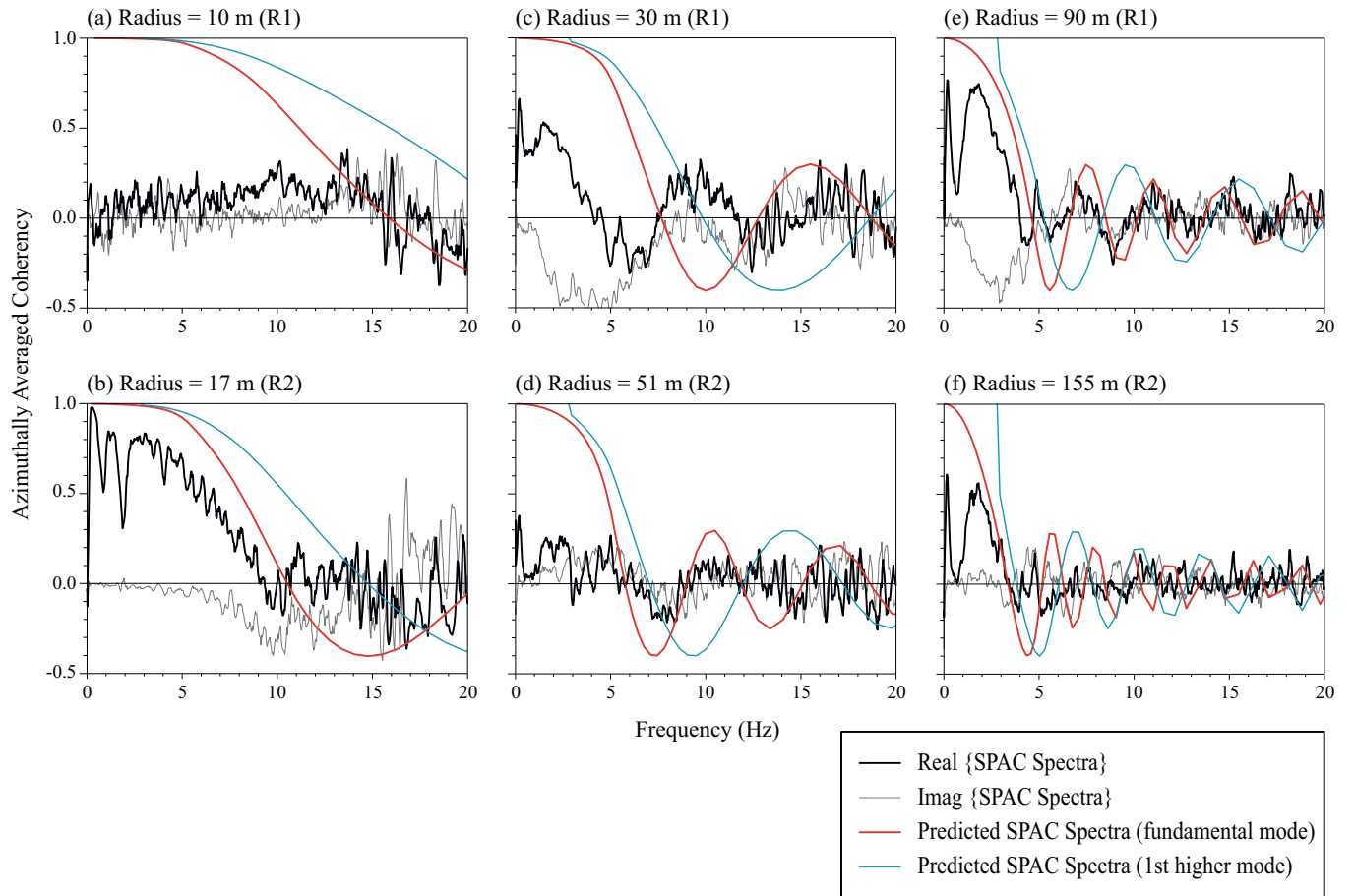


Figure A.6. *Site CCH*

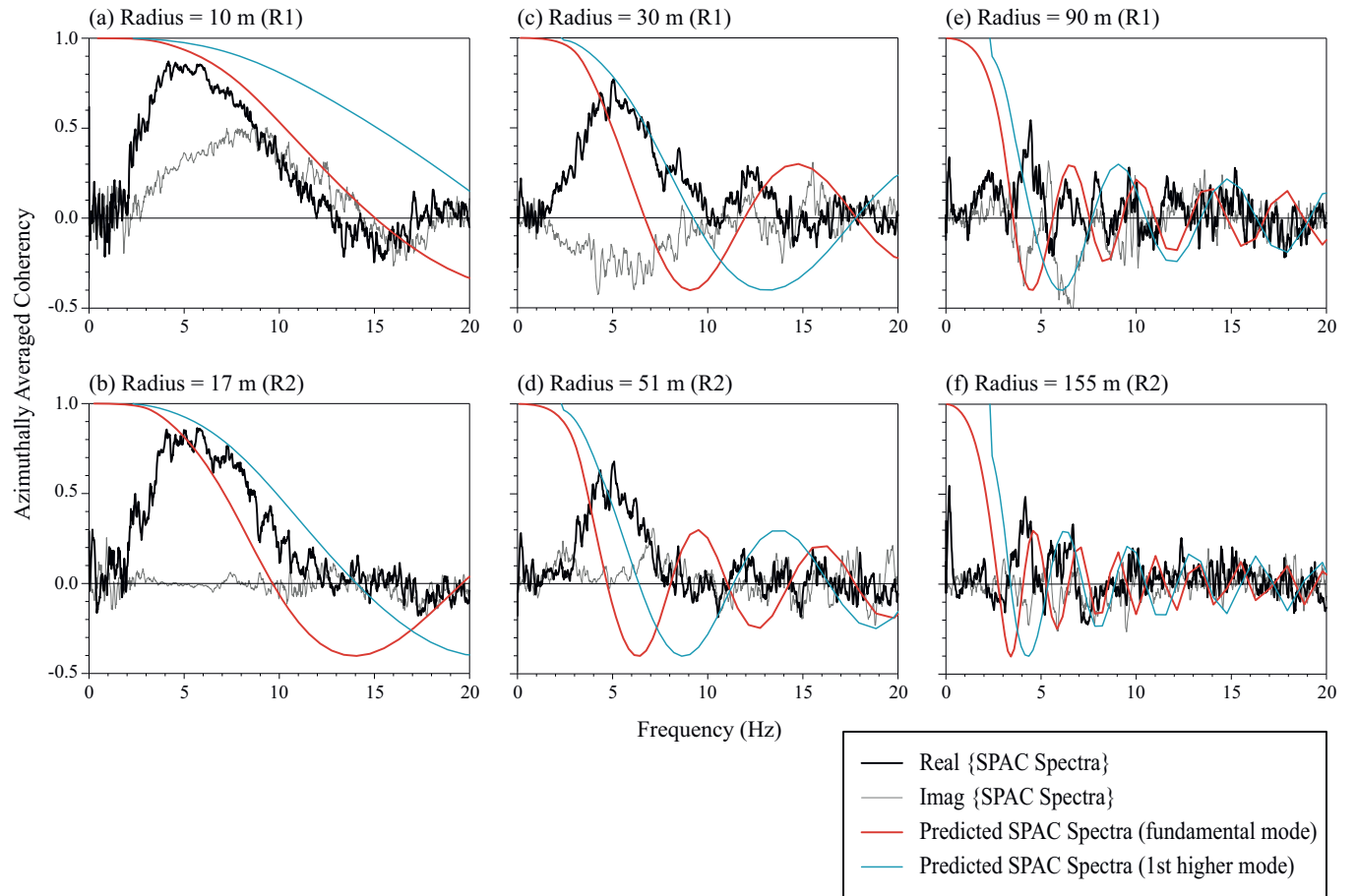


Figure A.7. *Site CCP*

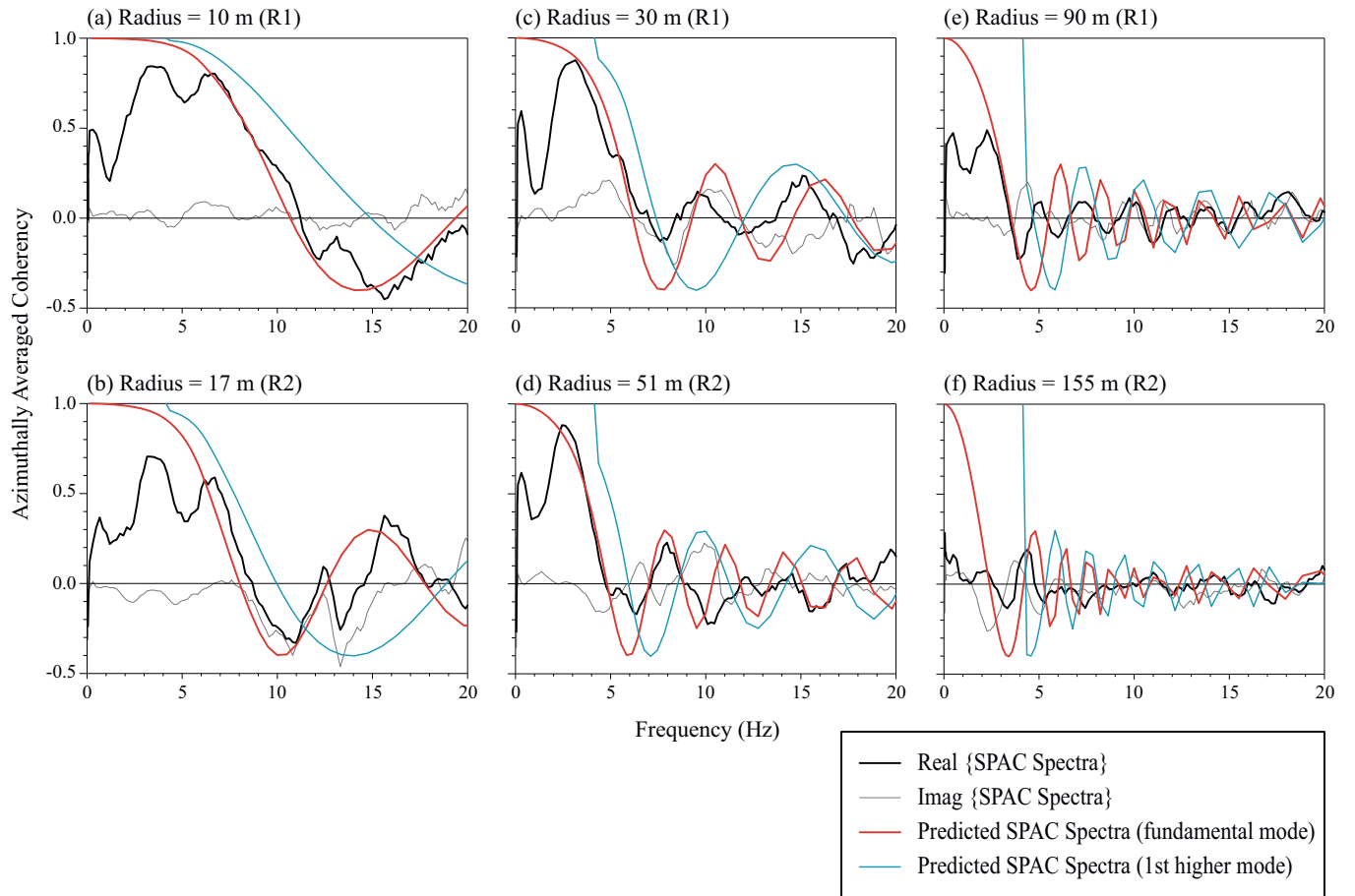


Figure A.8. *Site CVMS*

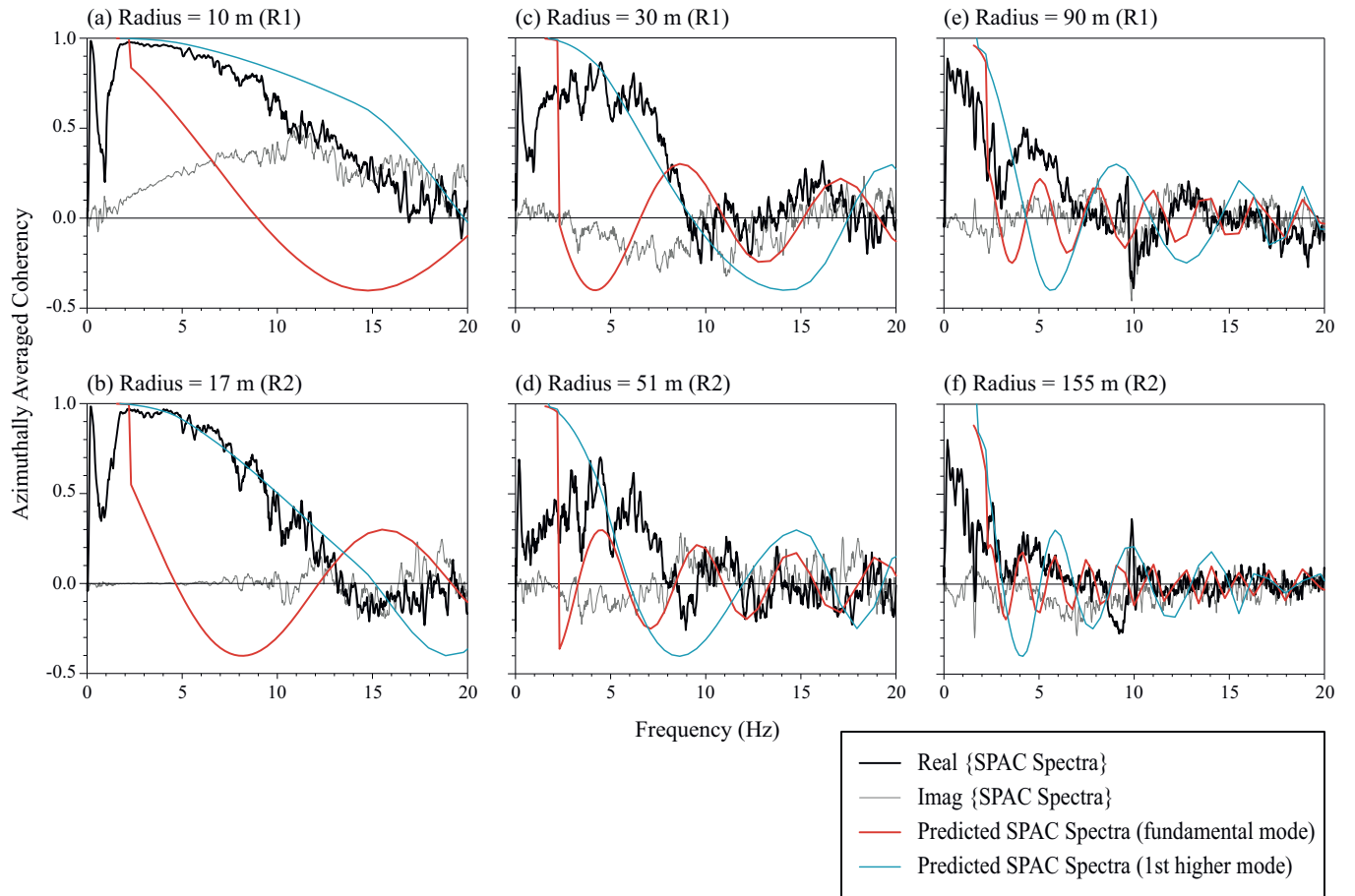


Figure A.9. *Site FRS*

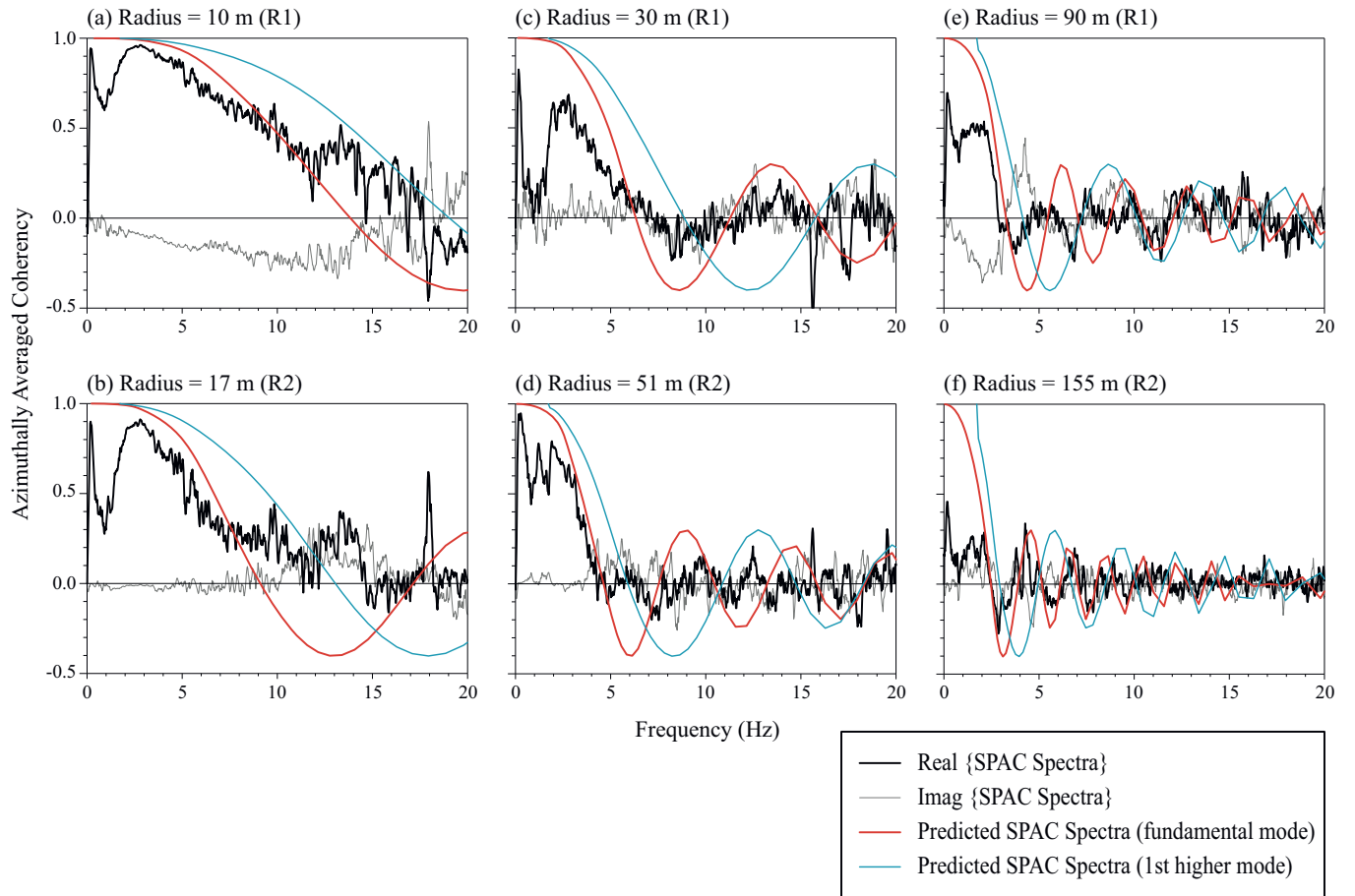


Figure A.10. *Site RES*

REFERENCES

- Albarelo, D., and E. Lunedei, (2010). Alternative interpretations of horizontal to vertical spectral ratios of ambient vibrations: new insights from theoretical modeling, *Bull. Earthquake Eng.*, **8**, 519-534, doi: 10.1007/s10518-009-9110-0.
- Aki, K. (1957). Space and time spectra of stationary stochastic waves, with special reference to microtremors, *Bull. Earthquake Res. Inst.*, **35**, 415-457.
- Arai, H., and K. Tokimatsu (2004). S-Wave Velocity Profiling by Inversion of Microtremor H/V Spectrum, *Bull. Seism. Soc. Am.*, **94**, 53-63, doi: 10.1785/0120030028.
- Arai, H., and K. Tokimatsu (2005). S-wave velocity profiling by inversion of microtremor dispersion curve and horizontal-to-vertical (H/V) spectrum, *Bull. Seism. Soc. Am.* **95**, 1766 - 1778.
- Asten, M. (2004). Optimised Array Design For Microtremor Array Studies Applied to Site Classification; Comparison of Results with SCPT Logs, *13th World Conference on Earthquake Engineering*, Vancouver, B.C., Canada, August 1-6, Paper No.2903.
- Asten, M., and D. Boore (2005). Microtremor methods applied to hazard site zonation in the Santa Clara Valley, *Seimol. Res. Lett.*, **76**, 257.
- Asten, M. (2006). Site shear velocity profile interpretation from microtremor array data by direct fitting of SPAC curves, *Third International Symposium on the Effects of Surface Geology on Seismic Motion*, Grenoble, France, Aug. 30 Sept. 1, Paper No. 99.
- Bonnefoy-Claudet, S., C.Cornou, P.Y. Bard, F. Cotton, P. Moczo, J. Kristek, and D. Fäh (2006). H/V ratio: A tool for site effects evaluation. Results from 1-D noise simulations, *Geophysical J. Int.*, **167**, 827-837.
- Bonnefoy-Claudet, S., A.Köhler, C. Cornou, M. Wathelet, P. Y. Bard (2008). Effects of Love Waves on Microtremor H/V Ratio, *Bull. Seism. Soc. Am.*, **98**, 288-300, doi: 10.1785/0120070063.
- Boore, D. and W. Asten (2008). Comparisons of Shear - Wave Slowness in the Santa Clara Valley, California, Using Blind Interpretations of Data from Invasive and Noninvasive Methods, *Bull. Seism. Soc. Am.*, **98**, 1983-2003, doi: 10.1785/0120070277.

- Borcherdt, R. D. (1970). Effects of local geology on ground motion near San Francisco Bay, *Bull. Seism. Soc. Am.*, **60**, 29-61.
- Borcherdt, R. D. (1994). Estimates of Site-Dependent Response Spectra for Design (Methodology and Justification). *Earthquake Spectra*, **10**, 617 - 653.
- Chávez-García, M. Rodríguez, and W. Stephenson (2005). An Alternative Approach to the SPAC Analysis of Microtremors: Exploiting Stationarity of Noise, *Bull. Seism. Soc. Am.*, **95**, 277-293, doi: 10.1785/0120030179.2005.
- Chávez-García F. J., M. Rodríguez and W. R. Stephenson (2006). Subsoil structure using SPAC measurements along a line, *Bull. Seism. Soc. Am.*, **96**, 729 - 736.
- Cramer, C.H. (2009). NEHRP site class amplification vs. site profile amplification in the CUS, *Seimol. Res. Lett.*, **80**, 365.
- Eisinger, C. (1998). A summary of the geology and hydrogeology of the Cedar Valley drainage basin, Iron County, Utah, *Utah Geological Survey Open-File Report 360*, Utah Dept. of Natural Resources. 15 p.
- Fäh, D., F. Kind, and D. Giardini (2001). A theoretical investigation of average H/V ratios, *Geophysical J. Int.*, **145**, 535-549.
- Fäh, D., F. Kind, and D. Giardini (2003). Inversion of local S-wave velocity structures from average H/V ratios, and their use for the estimation of site-effects, *J. Seism.*, **7**, 449-467, doi: 10.1023/B:JOSE.0000005712.86058.42.
- Governors Report (2010). Economic Report to the Governor, State of Utah Gary R. Herbert, Governor: Online <http://www.governor.utah.gov/dea/ERG/2010ERG.pdf>, accessed October 22, 2010.
- Higgins, J.M., and G. C. Willis (1995). Interim geologic map of the St. George quadrangle, Washington County, Utah, *Utah Geological Survey Open-File Report 323*, 97 p.
- Köhler, A., M. Ohrnberger, G. Scherbaum, M. Wathelet, and C. Cornou (2007). Assessing the reliability of the modified three-component spatial autocorrelation technique, *Geophys. J. Int.*, **168**, 779-796,
- Lachet, C. and P. Y. Bard (1994). Numerical and theoretical investigations on the possibilities and limitations of Nakamuras technique, *J. Phys. Earth.*, **42**, 377-397.
- Louie, J. N. (2001). Faster, better: Shear-wave velocity to 100 meters depth from refraction microtremors analysis, *Bull. Seism. Soc. Am.* **91**, 347-364

Lund, W., T.R. Knudsen, G.S. Vice, and L.M. Shaw (2008). Geologic Hazards and Adverse Construction Conditions. St. George-Hurricane Metropolitan Area, Washington County, Utah, *Utah Geological Survey, Special Study 127*, Utah Dept. of Natural Resources, 105 P.

Nakamura, Y. (1989). A method for dynamic characteristics estimation of sub-surface using microtremor on the ground surface, *Q. Rept. Railway Tech. Res. Inst.* **30**, 25-33.

Nakamura, Y. (1996). Real-time information systems for hazards mitigation, *Proceedings of the 11th World Conference on Earthquake Engineering*, Acapulco, Mexico.

Nakamura, Y. (2000). Clear identification of fundamental idea of Nakamura technique and its applications, *Proceedings of the 12th World Conference on Earthquake Engineering*, Auckland, New Zealand.

Nogoshi, M., and T. Igrashi (1971). On the propagation characteristics of microtremors, *J. Seism. Soc. Japan* **23**, 264-280.

Okada, H. (2001). Remarks on the efficient number of observation points for the spatial auto-correlation method applied to array observations of micro tremors, *Proc. Of the 104th SEGJ Conf., Society of Exploration Geophysicists, Japan* (in Japanese).

Okada, H., (2003). The Microtremor Survey Method, *Society of Exploration Geophysicists of Japan, Translated by K. Suto, Geophysical Monograph Series No. 12*, Society of Exploration Geophysicists.

Park, S. and S. Elrick (1998). Predictions of shear - wave velocities in southern California using surface geology, *Bull. Seism. Soc. Am.*, **88**, 677-685.

Pechmann, J. C., W. J. Arabasz, and S. J. Nava (1995). Seismology in Christenson, G. E., editor, The September 2, 1992, ML 5.8 St. George earthquake, *Utah Geological Survey Circular*, **88**, p. 1.

Poggi, V., and D. Fäh (2010). Estimating Rayleigh wave particle motion from three-component array analysis of ambient vibrations, *Geophys. J. Int.*, **180**, 251-267.

Ritsema, J. and T. Lay (1995). Long-period regional wave moment tensor inversion for earthquakes in the western United States, *J. Geophys. Res.*, **100**, 9853-9864, doi:10.1029/95JB00238.

Rowley, P.D., V. S. Williams, G. S. Vice, D. J. Maxwell, D. B. Hacker, L. W. Snee, and J. H. Mackin (2006). Interim geologic map of the Cedar City 30×60 quadrangle, Iron and Washington Counties, Utah, *Utah Geological Survey Open-File Report 476DM*, 23 p. pamphlet, scale 1:100,000.

Singh, S. K., J. Lermo, T. Dominguez, M. Ordaz, J. M. Espinosa, E. Mena, et al. (1998). The Mexico earthquake of September 19, 1985 - a study of seismic waves in the valley of Mexico with respect to a hill zone site, *Earthquake Spectra*, **4**, 653 - 673.

Stephenson, J., S. Hartzell, A.D. Frankel, M. Asten, D. L. Carver, W. Y. Kim (2009). Site characterization for urban seismic hazards in lower Manhattan, New York City, from microtremor array analysis, *Geophys. Res. Lett.*, **36**, doi:10.1029/2008GL036444.

Wessel, P. and W. H. F. Smith (1998). New, improved version of the Generic Mapping Tools released, *Eos Trans. AGU*, **79**, 579.